Physics of Fluids ARTICLE scitation.org/journal/phf

Investigation into the coherence of flame intensity oscillations in a model multi-element rocket combustor using complex networks

Cite as: Phys. Fluids **34**, 034107 (2022); doi: 10.1063/5.0080874
Submitted: 4 December 2021 · Accepted: 20 February 2022 ·
Published Online: 3 March 2022

Praveen Kasthuri,[1] Abin Krishnan,[2] Rohan Gejji,[3] William Anderson,[3] Norbert Marwan,[4] Jürgen Kurths,[4,5] and R. I. Sujith[1,a)]

AFFILIATIONS

[1]Department of Aerospace Engineering, Indian Institute of Technology Madras, Chennai 600036, India
[2]Department of Mechanical Engineering, School of Engineering, Cochin University of Science and Technology, Cochin 682022, India
[3]School of Aeronautics and Astronautics, Purdue University, West Lafayette, Indiana 47907, USA
[4]Potsdam Institute for Climate Impact Research, Potsdam 14473, Germany
[5]Department of Physics, Humboldt University, Berlin 12489, Germany

[a)]**Author to whom correspondence should be addressed:** sujith@iitm.ac.in

ABSTRACT

Capturing the complex spatiotemporal flame dynamics inside a rocket combustor is essential to validate high-fidelity simulations for developing high-performance rocket engines. Utilizing tools from a complex network theory, we construct positively and negatively correlated weighted networks from methylidyne (CH^*) chemiluminescence intensity oscillations for different dynamical states observed during the transition to thermoacoustic instability (TAI) in a subscale multi-element rocket combustor. We find that the distribution of network measures quantitatively captures the extent of coherence in the flame dynamics. We discover that regions with highly correlated flame intensity oscillations tend to connect with other regions exhibiting highly correlated flame intensity oscillations. This phenomenon, known as assortative mixing, leads to a core group (a cluster) in the flow-field that acts as a "reservoir" for coherent flame intensity oscillations. Spatiotemporal features described in this study can be used to understand the self-excited flame response during the transition to TAI and validate high-fidelity simulations essential for developing high-performance rocket engines.

I. INTRODUCTION

Thermoacoustic instability (TAI) continues to hinder the development of rocket engines aimed for space and other strategic applications.[1–4] This phenomenon is characterized by extremely large amplitude pressure and heat release rate oscillations in the combustor. These large amplitude oscillations entail premature structural failure of engine components, overwhelm the thermal protection system due to excessive heat transfer, and can even lead to total mission failure. As a result, there is substantial interest in studies that enhance our knowledge on the temporal and spatiotemporal dynamics of thermoacoustic instabilities occurring inside rocket combustors and toward designing control remedies to overcome this hazardous phenomenon.[5]

In a typical liquid rocket combustor, the fuel and oxidizer are supplied to the combustor through a number of carefully arranged injectors to achieve the desired mixture required for combustion. The propellants rapidly react in the high pressure environment of the combustor establishing a multitude of jet flames. Depending on the spatiotemporal interaction of the combustion and flow-field with the acoustic field, thermoacoustic instability characterized by either low or high frequency oscillations can be established. Especially, the occurrence of high-frequency thermoacoustic oscillations is hazardous due to extreme wall heat transfer resulting in catastrophic failures.[6]

A number of studies have focused on characterizing high frequency thermoacoustic oscillations applied to liquid rocket propulsion.[7–9] Understanding the flame dynamics in conjunction with the acoustic pressure oscillations forms the fundamental part of many of these studies.[6,9–11] The jet flame dynamics is controlled by local acoustic perturbations, turbulent flow, non-premixed combustion, hydrodynamic instabilities, and the geometry of the combustor.

The heat release rate oscillations can be separated into two components: coherent and incoherent fluctuations.[12] The jet flame usually exhibits intrinsic incoherent oscillations in response to the turbulent flow fluctuations.[12] Based on the flame density ratio, the jet flame may exhibit coherent oscillations.[13] Furthermore, when the jet flames are sensitive to the local transverse acoustic pressure and acoustic velocity fluctuations, they are laterally displaced and oscillate vigorously.[14–16] In a rocket combustor susceptible to transverse thermoacoustic instability, the neighboring jet flames might merge and even exhibit strong collective interactions.[17] Such flame–flame interactions have been proposed to be a possible driving mechanism for thermoacoustic instability.[18,19] Furthermore, the presence of atomization, vortex shedding, shear layers, coherent structures, and shock waves in the flow-field imparts heterogeneity to the local flame dynamics. Therefore, the jet flame dynamics in a rocket combustor is heavily influenced by the nonlinear interactions among acoustic, combustion, and fluid mechanic processes.

Due to the complex nonlinear interactions between these various physical processes, there is an emergent behavior in the spatiotemporal flame dynamics that cannot be understood using the framework of a linear theory. Therefore, it is essential to study the flame dynamics under the purview of the complex systems approach.[20] Here, the emphasis is on understanding the system as a whole, instead of examining the components in isolation. In this work, we base our analysis on the complex networks approach, which provides a framework compatible with the complex system viewpoint. Complex network analysis is a promising approach to understand the complex behavior of several real-world complex systems in which interactions between different subsystems lead to critical transitions, self-organization, collective behavior, cascading failures, etc.[21] In the complex network theory, the components and interactions among them are represented as nodes and links, respectively. Since its inception, complex networks have been applied to diverse areas such as medicine, earth sciences, economics, biology, computer science, and fluid mechanics.[21–23]

Recent studies conducted on air-breathing turbulent combustors have adopted the complex network theory to understand the temporal and spatiotemporal dynamics during the transition from a stable state to thermoacoustic instability via intermittency (INT).[24] Specifically, the networks constructed from temporal acoustic pressure oscillations characterized the network topology and provided precursors to thermoacoustic instability[25,26] and lean blowout.[27] Hybrid approaches combining machine learning and complex networks have been useful to devise precursors for thermoacoustic instabilities.[28] Analyzing acoustic pressure data acquired from the same model rocket combustor used in this study, Kasthuri *et al.*[29] used recurrence networks to show the slow-fast timescales arising due to the phenomenon of wave steepening.

Unni *et al.*[30] identified "critical regions" in the flow-field for each dynamical state during the transition to thermoacoustic instability using spatial networks based on the correlation between the time series of velocity fluctuations at different locations in a bluff-body stabilized combustor. For the same combustor, Krishnan *et al.*[31,32] experimentally showed that the 'critical region', identified using the network theory, is the optimal location for implementing passive control strategies. They also constructed time-varying spatial networks to quantify the spatiotemporal evolution of clusters of acoustic power sources during the transition to thermoacoustic instability.[33] Hashimoto *et al.*[34] devised a turbulence network from vorticity to characterize the spatiotemporal dynamics during thermoacoustic instability and identified regions driving thermoacoustic instability in a model rocket combustor. Aoki *et al.*[35] used the network entropy in ordinal transition partition networks to detect the dynamical states in the same combustor. Recently, Shima *et al.*[36] used a thermoacoustic power network to understand the role of thermoacoustic power sources in driving of thermoacoustic oscillations.

In light of the advancements in the complex network theory, in this paper, we construct positively and negatively correlated spatial networks to identify different regions of coherent and incoherent heat release rate oscillations in the turbulent reactive flow-field of a 2D subscale rocket combustor exhibiting self-excited transverse instabilities. Since coherent flame oscillations can generate and sustain thermoacoustic instability,[12,37] it is of utmost importance to characterize the coherence in the flame oscillations. Positively and negatively correlated flame regions might indicate the locations of sources or sinks of acoustic power, respectively. In turn, the acoustic power sources and sinks promote or inhibit the thermoacoustic oscillations present in the combustor. Moreover, the magnitude of positive or negative correlation observed at different spatial locations allows us to distinguish different spatial regions in the reactive flow-field. Understanding the extent and spatial distribution of positively and negatively correlated regions during the transition to thermoacoustic instability forms the core motivation behind this study.

The remainder of this paper is structured as follows: first, we describe the experimental model rocket combustor in Sec. II. Then, we describe the methodology behind network construction in Sec. III. Subsequently, using the network measures described in Sec. IV, we quantify the extent of coherence and incoherence in the flame intensity oscillations at different regions in the combustor in Sec. V.

II. EXPERIMENTAL SETUP

The multi-element model rocket combustor is based on an oxidizer-rich staged combustion cycle (Fig. 1). Gaseous oxygen preheated to $T_{O_2} = 620\,\mathrm{K}$ in a preburner and methane at $T_{CH_4} = 297\,\mathrm{K}$ are fed to the combustor though an oxidizer post maintaining a mean Mach number of 0.265 at nominal operating conditions. The combustor contains a linear array of nine equispaced oxidizer centered gas-gas shear coaxial injectors located at the downstream end of the oxidizer posts. Methane is introduced into the combustor through each of these nine shear coaxial injectors while a choked inlet condition is maintained to ensure a steady flow rate of methane. Therefore, a non-premixed turbulent jet flame is established at the exit of each injector. The corresponding Reynolds number estimated at the injector exit is $\sim 3.93 \times 10^5$.

The reactant flow rates were optimized to achieve an equivalence ratio (ϕ) of ~1.24, representative of oxidizer-rich staged combustion cycle based rocket engines. A mean pressure level (P_c) of ~1.14 MPa is maintained over the course of a test. The combustor walls are coated with a protective layer of thermal barrier coating to minimize the wall heat loss during the test interval. The cumulative mass flow rate of oxidizer ($\dot{m}_{O_2}$) is 0.71 kg/s, while the mass flow rate of methane ($\dot{m}_{CH_4}$) is maintained at 0.22 kg/s. The uncertainty in the reactant mass flow rates was $\leq 1\%$ with a 95% confidence interval.

The geometry and operating conditions were optimized to excite only the transverse acoustic modes with a fundamental mode

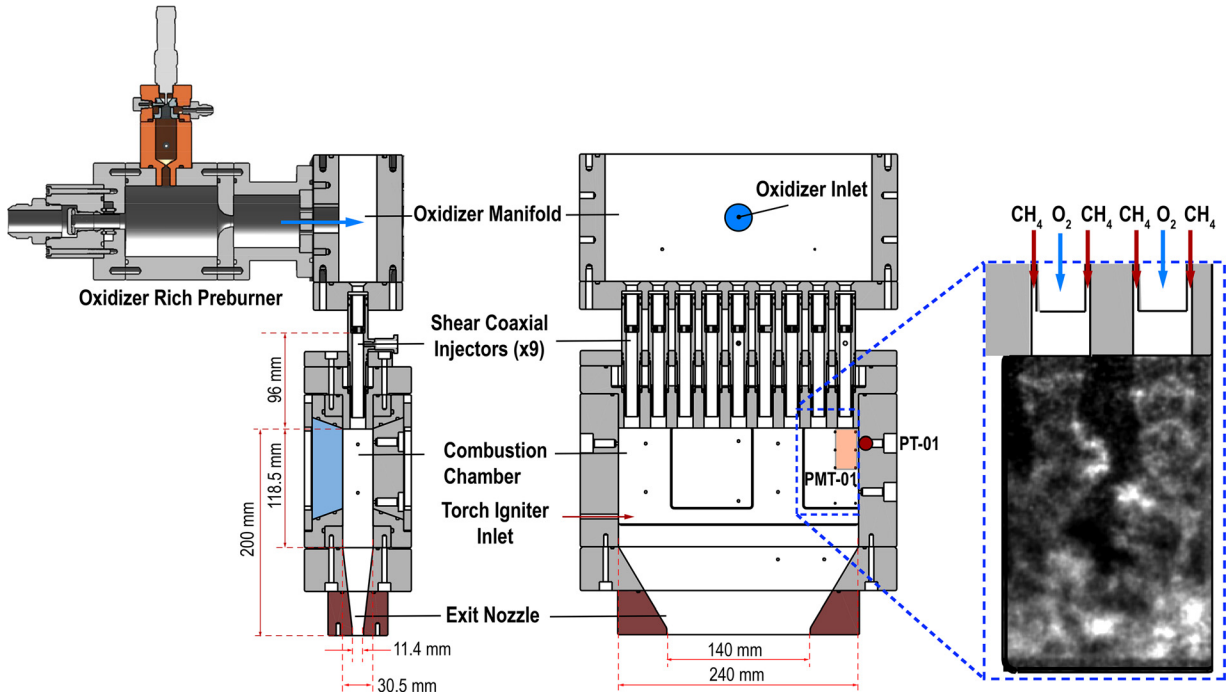

FIG. 1. Schematic of the model multi-element rocket combustor along with the representative CH* chemiluminescence image obtained from the optically accessible window located near the end wall.

frequency (f_{1T}) of 2650 Hz in the combustor. A nozzle at the end of the converging section ensured a choked boundary condition at the exit of the combustor, thus isolating the acoustic wave propagation to the main combustion chamber and injector manifolds. A test run providing approximately 1 s of steady inflow provides sufficient time to acquire data exhibiting transition to thermoacoustic instability at the frequencies of interest with negligible effects of heat loss. A summary of operating conditions relevant to the current work is provided in Table. I.

In this study, we are interested in the flame dynamics near the wall, where the acoustic pressure and heat release rate oscillations are the highest.[38] As a result, we analyze the methylidyne (CH*) intensity oscillations emanating from the two turbulent jet flames located toward one end of the combustor through an optically accessible window. We acquire the acoustic pressure oscillations (using piezoresistive Kulite WCT-312M sensor) at the right-side end wall at a rate of 250 kHz. The pressure sensors are mounted in a recessed Helmholtz cavity to provide thermal isolation from the hot combustion gases. This installation enables accurate measurement of dynamic pressure fluctuations in the chamber while reducing the thermal load on the sensor element.[39]

TABLE I. Summary of the operating conditions.

$\dot{m}_{O_2}$ (kg/s)	$\dot{m}_{CH_4}$ (kg/s)	ϕ (–)	P_c (MPa)	T_{O_2} (K)	T_{CH_4} (K)	f_{1T} (Hz)
0.71	0.22	1.24	1.14	620	297	2650

Currently, it is impractical to derive the heat release rate measurements directly from experiments performed at elevated pressures due to the dependence of chemiluminescent emission on the pressure, strain rate, and turbulence level.[40,41] Therefore, chemiluminescence emission of short-lived species, such as methylidyne (CH*) and hydroxyl (OH*), can be used as an indirect measure of the heat release rate.[41]

In this work, without modeling the flame dynamics in the turbulent flow-field, we rely on the intensity oscillations acquired from CH* chemiluminescence to study the coherence in the jet flame dynamics. The CH* chemiluminescence images, focused on the optically accessible window located near the end wall, are acquired at a rate of 100 kHz simultaneously with pressure measurements. An optical filter (Semrock 434/14 Brightline Bandpass) of 434 ± 14 nm bandwidth isolated CH* emissions from the overall luminosity. The emissions are collected through a 200 mm focal length, *f*/4.0 objective (Nikon AF Micro NIKKOR) and intensified by a Lambert HiCATT 25 intensifier with a 1:1 relay lens. The images are recorded using a Phantom v2512 high speed CMOS camera with a pixel density of 0.214 mm/pixel, rendering a spatial resolution of 126 px × 78 px. More detailed descriptions of the geometry of this experimental setup, the operating conditions, the measurement techniques, and associated uncertainties can be found in previous works.[42–44]

III. METHODOLOGY OF NETWORK CONSTRUCTION

In this study, each spatial location (i.e., each pixel) in the region of interest is considered as a node. The interactions between any two nodes are captured by the links connecting them. To quantify the interaction between two such nodes, various measures, such as

Pearson correlation, average mutual information, and event synchronization between two time series, have been used to construct relevant spatial networks.[22]

Here, we construct weighted networks based on the Pearson correlation [Eq. (1)] between the time series of intensity fluctuations obtained from the CH^* chemiluminescence images acquired from the combustor as indicated in Fig. 1. Pearson correlation (R_p) is a linear measure computed between two time series. A positive R_p suggests that the two time series increase and decrease together, whereas a negative R_p indicates that one time series increases while the other decreases and vice versa. The case of $R_p = 0$ means that there is no linear relationship between the two time series over the time interval considered. In Eq. (1), x_i^t and x_j^t are the elements of the two time series at their corresponding grid points, whose arithmetic mean is given by $\overline{x_i}$ and $\overline{x_j}$, respectively,

$$R_p(i,j) = \frac{\sum_{t=1}^{n}\left(x_i^t - \overline{x_i}\right)\left(x_j^t - \overline{x_j}\right)}{\sqrt{\sum_{t=1}^{n}\left(x_i^t - \overline{x_i}\right)^2}\sqrt{\sum_{i=1}^{t}\left(x_j^t - \overline{x_j}\right)^2}}. \tag{1}$$

Here, n is the total number of time instants used to evaluate the time-averaged correlation (R_p). We have a total of $N = 9828$ (126 px × 78 px) nodes with $i, j \in [0, N]$. We compute the pairwise correlation values (R_p) for all the nodes and encapsulate this information in a correlation matrix of size $N \times N$. Then, we construct positively ($R_p > 0$) and negatively ($R_p < 0$) correlated weighted networks from the correlation matrix made up of R_p for all pairwise combinations of the available spatial locations. For the positively correlated network, we set all negative correlation coefficients to zero. While analyzing the negatively correlated network, we set all positive correlation coefficients to zero and then take the absolute value of the correlation matrix to obtain the negatively correlated network. Then, we can proceed to set the appropriate positive threshold (ε) to disregard weaker correlations and build the relevant adjacency matrix. The rationale behind the selection of ε followed in this study is described in Sec. V B.

The adjacency matrix, A_{ij} ($N \times N$) encodes the connections between all the grid points in the network. Two nodes, i and j, are connected, and $R_p(i,j)$ is assigned as the corresponding weight (W_{ij}) of their link, only when $R_p(i,j)$ exceeds a predefined threshold, ε. The positively (A_{ij}^+) and negatively (A_{ij}^-) correlated adjacency matrices are generated following Eq. (2). We do not consider self-connections rendering $A_{ii} = 0$. In this manner, we construct a spatial network for each of the dynamical states observed in the combustor

$$A_{ij}^+ = \begin{cases} W_{ij} = R_p(i,j), & \text{if } R_p(i,j) \geq \varepsilon, \\ W_{ij} = 0, & \text{otherwise}, \end{cases} \tag{2.1}$$

$$A_{ij}^- = \begin{cases} W_{ij} = -R_p(i,j), & \text{if } -R_p(i,j) \geq \varepsilon, \\ W_{ij} = 0, & \text{otherwise}. \end{cases} \tag{2.2}$$

IV. NETWORK MEASURES TO QUANTIFY THE SPATIAL DYNAMICS FOR EACH DYNAMICAL STATE

We use network measures, such as degree, node strength, and average nearest neighbors' degree, to compare the topology of networks for each dynamical state. The degree, k_i [Eq. (3)], quantifies the number of grid points (nodes) connected to a particular grid point i in the network[21]

$$k_i = \sum_{j=1}^{N} nnz(A_{ij}). \tag{3}$$

Here, the nnz function counts the number of non-zero elements present in each row in the adjacency matrix. The degree distribution, $P(k)$ vs k, represents the probability that a node in a network has degree k. If n_k represents the number of nodes having degree k, $P(k)$ is defined as $P(k) = n_k/N$.

The node strength s_i for node i captures the sum of the weights of all its links

$$s_i = \sum_{j \in N} W_{ij}. \tag{4}$$

Both k_i and s_i quantify the relative importance of node i in the network. However, s distinguishes nodes based on the weight of the links, rather than on the number of links.

The behavior of a node can be significantly influenced by its spatial location. The interactions among neighboring nodes result in degree correlations in the network. To probe the presence of degree correlations, it is important to analyze the neighbors of a node. We quantify the effect of neighboring nodes by the average degree of the nearest neighbors[45] of node i, which is evaluated as

$$k_{nn,i} = \frac{1}{k_i}\sum_{j \in \nu(i)} k_j. \tag{5}$$

Here, ν_i covers only the nearest neighbors (nn) of node i. Then, the degree correlation function ($k_{nn}(k)$) is evaluated from k_{nn} as

$$k_{nn}(k) = \sum_{k'} k' P(k'|k), \tag{6}$$

where $P(k'|k)$ is the conditional probability that a k-degree node is connected to a k'-degree node.[21] Thus, $k_{nn}(k)$ is the average degree of the neighbors of all k-degree nodes.

The variation of $k_{nn}(k)$ with k unearths correlations between the neighbors.[46] An increasing trend of $k_{nn}(k)$ is termed as assortative and suggests that high degree nodes tend to be surrounded by other high degree nodes. In simple words, it quantifies the "rich gets richer" effect.[21] In contrast, a decreasing trend is termed as disassortative.[21] Networks exhibiting no clear distinguishable trend in the distribution of $k_{nn}(k)$ are called neutral networks.[21] Using the aforementioned measures, we characterize the spatial weighted positively and negatively correlated networks during the transition to thermoacoustic instability.

V. RESULTS AND DISCUSSION

Before constructing and analyzing the weighted correlation networks, we briefly discuss different dynamical states occurring in the combustor. In Fig. 2, we plot the time series of pressure measured at the end wall of the combustor along with its scalogram encoding the time-frequency behavior. In total, we observe two dynamical states: intermittency followed by thermoacoustic instability. Thermoacoustic instability is characterized by large amplitude periodic oscillations. In the scalogram, we observe multiple transverse acoustic frequencies

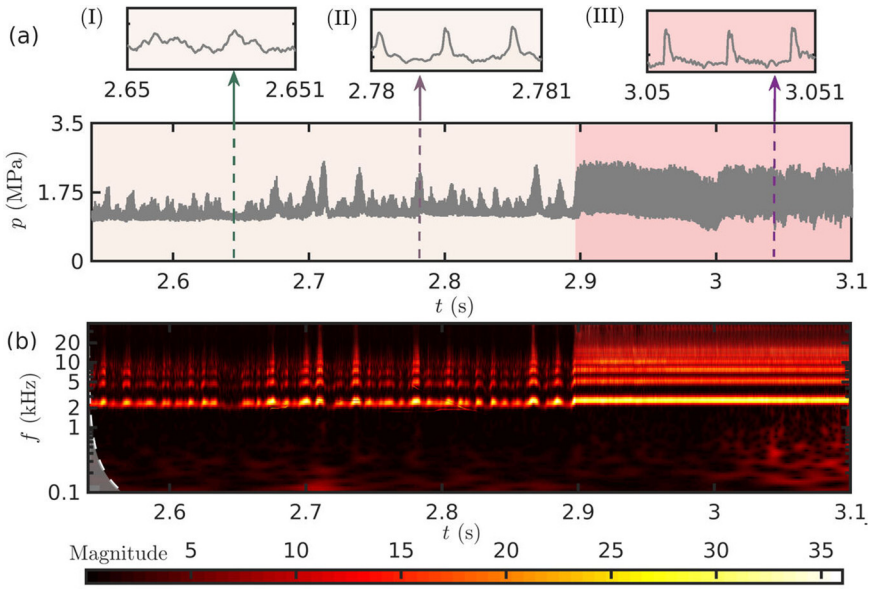

FIG. 2. (a) Time series of the acoustic pressure (p) along with its zoomed insets during (I) aperiodic epoch of intermittency, (II) periodic epoch of intermittency, and (III) thermoacoustic instability. (b) The corresponding scalogram showing the frequency-time behavior during the transition from intermittency to thermoacoustic instability. Note that the abscissa is logarithmically scaled.

excited during thermoacoustic instability. However, the dominant frequency of the oscillations at the end wall corresponds to the first transverse mode (1 T mode at ∼2650 Hz). On the other hand, intermittency is featured by bursts of large amplitude periodic oscillations occurring amid low amplitude aperiodic oscillations.[43,47] The aperiodic and periodic epochs during intermittency can be clearly distinguished in the scalogram. A detailed analysis of the temporal variation of acoustic pressure using tools from the dynamical systems theory is present in our earlier work.[43]

During the periodic epochs of intermittency and thermoacoustic instability, we also observe a shock wave propagating in the transverse direction (i.e., perpendicular to the main flow direction) in the combustor. The speed of the shock wave matches closely with the characteristic transverse acoustic timescale (1 T mode) of the combustor. The passage of this shock wave imparts a transverse displacement on each of the jet flames. In turn, a periodic steepened waveform[43] is engendered in the pressure and local flame intensity oscillations during thermoacoustic instability. Next, we will describe the spatiotemporal behavior of the jet flames observed during intermittency and thermoacoustic instability.

A. Flame dynamics during intermittency and thermoacoustic instability

Due to the periodicity in the local intensity oscillations, it is appropriate to understand the flame behavior during periodic epochs of intermittency and thermoacoustic instability by adopting the method of phase averaging.[48] In this method, only the images pertaining to a particular phase are averaged over the time interval of interest. We cannot apply phase averaging during the stable state and for aperiodic epochs of intermittency, since the phase for aperiodic oscillations cannot be properly defined. Four phase-averaged CH^* chemiluminescence images during the periodic epochs of intermittency and thermoacoustic instability in the combustor are shown in Fig. 3. Four phases (A–D), indicated over the pressure waveform in Figs. 3(a) and 3(b), are selected to describe the dynamic behavior of the jet flames during their respective dynamical states.

During periodic epochs of intermittency [see Fig. 3(c)], the jet flames continue to be distinguishable from each other, irrespective of the phase. We observe that the jet flames during intermittency exhibit higher intensities when the passage of the shock wave coincides with the peak pressure (captured by phase at A), whereas the minimum flame intensity coincides with the pressure minima (captured by phase at C) during which the shock wave is far away the optical window. The images corresponding to phases B and D show intermediate flame intensities.

However, during thermoacoustic instability [see Fig. 3(d)], we observe significantly higher intensities coinciding with the local pressure maxima (phase A). Equivalently, the intensities are at their lowest during the pressure minima (phase C). Due to the large transverse oscillations during this state, we observe that the jet cores are no more intact, and the jet flames can no more be distinguished from their neighbors. As the shock wave passes through the jet flame, it imparts a large transverse displacement, substantially displaces the jet core, and momentarily results in a spike in the local flame intensity. This spike can be identified from the high intensities observed in the longitudinal location, where the jet flames impinge on the end wall [phase A in Fig. 3(d)]. After the shock wave passes through the jet flame, there is a longer relaxation period (phases B–D). This longer interval allows the fuel and oxidizer to mix and the jet core to regain its original shape. Moreover, during thermoacoustic instability, the jet flames that are compact near the injector spread out at the downstream locations. As a result, the mixing of propellants is enhanced by the secondary flows caused by vortical dissipation along the flame surfaces. Eventually, the mixed propellants auto-ignite leading to higher flame intensities, well downstream of the injector.[44] The temporal and spatiotemporal coupled interaction between the acoustic pressure oscillations and CH^* intensity oscillations for the test case described in this work is described in detail by Kasthuri *et al.*[38]

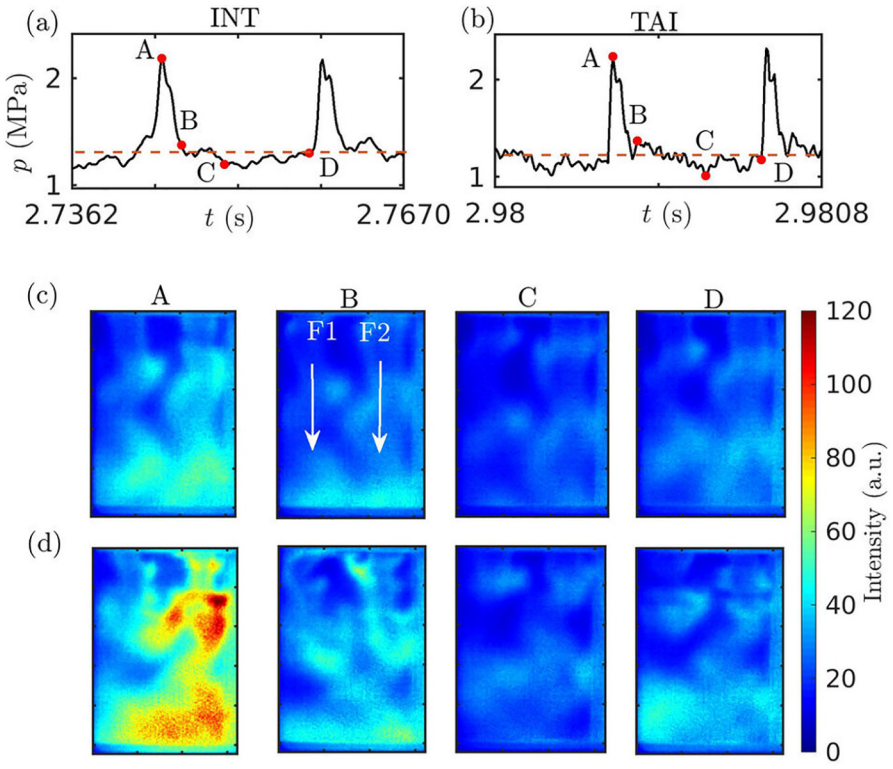

FIG. 3. Time series of acoustic pressure during (a) intermittency (INT) and (b) thermoacoustic instability (TAI). The four phases (A–D) at which the CH^* chemiluminescence images are averaged are marked over the time series. The phase-averaged images during (c) intermittency and (d) thermoacoustic instability are shown. The two jet flames visible through the optically accessible windows are marked in the phase averaged image (at B) during intermittency.

Next, we will evaluate the correlation between all the node pairs and build suitable weighted networks to study the coherence in the flame intensity oscillations recorded near the end wall of the combustor.

B. Coherence in the flame intensity oscillations

The extent of coherence (or incoherence) present in the flame intensity oscillations is quantified by the Pearson correlation [see Eq. (1)]. It is necessary to know the range of correlation values computed between the pairwise local intensity oscillations (i.e., node pairs) before network construction. With this aim, the empirical probability distribution of the correlation values, $P(R_p)$, observed for each dynamical state is presented in Fig. 4. During both the dynamical states, the range of values spanning positive correlation is wider than that of negative correlation. This observation suggests that most of the node pairs are positively correlated in the dynamics of flame intensity oscillations. The magnitude of the mean correlation increases from 0.25 during intermittency to 0.46 during thermoacoustic instability.

The distribution of the correlation values changes its form from a unimodal distribution (with peak R_p at 0.18) during intermittency to a bimodal distribution during thermoacoustic instability. We obtain a bimodal distribution (with two R_p peaks at 0.38 and 0.68) during thermoacoustic instability since the jet flames respond both to the incident and reflected shock waves for each cycle.

Since the selection of a suitable correlation threshold is non-trivial, we compute the positively and negatively correlated networks for different correlation thresholds (ε) to understand the varying levels of coherence in the flame intensity oscillations.

Selecting $\varepsilon = 0$ would allow us to examine either the effect of all positive or negative correlations for the positively or negatively correlated networks, respectively. Successive increments in ε would remove the weak correlations and reveal the effect of strong correlations in the dynamics of flame intensity oscillations in the combustor.

Next, we study the effect of short-range and long-range links on the extent of positive and negative correlations. In Fig. 5, we show all possible link weights (W_{ij}) for each Euclidean distance of the link (D_{ij})

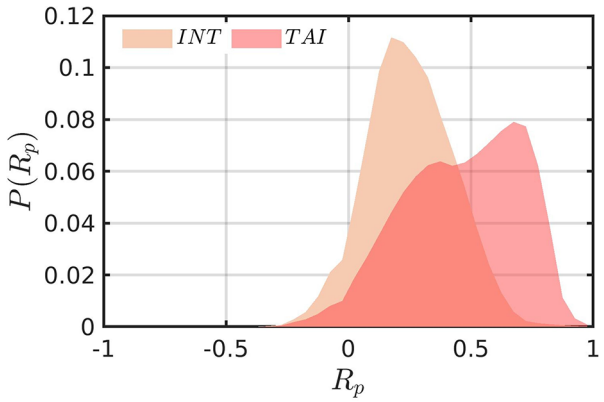

FIG. 4. Empirical probability distribution of correlation values observed during intermittency (INT) and thermoacoustic instability (TAI). The mean of the distribution increases during the transition to thermoacoustic instability indicative of the emergence of more coherent flame intensity oscillations.

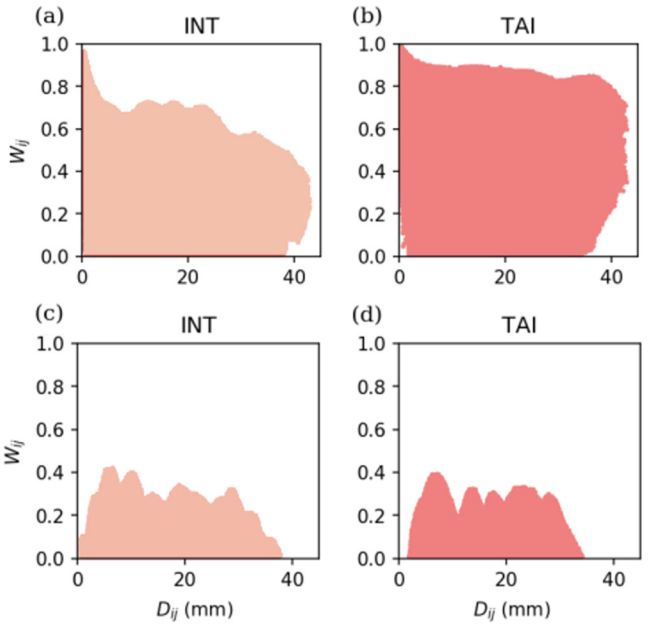

FIG. 5. Link weight (W_{ij}) vs the Euclidean link distance (D_{ij}) as obtained for the positively correlated network during (a) intermittency (INT), (b) thermoacoustic instability (TAI), and the negatively correlated network during (c) intermittency and (d) thermoacoustic instability. Positively correlated networks have strong long-range correlations, which are absent in negatively correlated networks.

during each dynamical state for the positively and negatively correlated networks. This plot reveals all the possible W_{ij} for a given D_{ij}. Hence, W_{ij} is multi-valued for a given D_{ij}. At this point, we reiterate that there are no self-connections, and therefore, for all $D_{ij} = 0$, $W_{ij} = 0$.

At the outset, we observe that the distributions of W_{ij} are similar during both intermittency and thermoacoustic instability. From the plots for the positively correlated network [Figs. 5(a) and 5(b)], we observe that the highest W_{ij} belong to the links connecting the nearest neighbors (i.e., the smallest D_{ij}). The presence of high W_{ij} at lower D_{ij} indicates strong local interactions resulting in higher correlation among nodes over a neighborhood. Interestingly, during thermoacoustic instability, we observe high values of W_{ij} that are greater than 0.8, even at larger D_{ij}. This observation suggests the presence of long-range widespread interactions among different local regions near the end wall of the combustor.

In a similar manner, all possible W_{ij} for each D_{ij} for the negatively correlated network corresponding to each dynamical state are plotted in Figs. 5(c) and 5(d). Here, across both the dynamical states, we observe that there are no connections to the nearest neighbors. Possibly, the presence of convection in the flow induces only positive correlations within the local neighborhood of a node. Maximum W_{ij} is observed not in the local neighborhood of the nodes but for links having intermediate D_{ij} values. The absence of negative correlation in the immediate neighborhood of a node suggests that convection induces only positive correlations. This reveals a fundamental difference in the connectivity of the positively and negatively correlated spatial networks. Hereon, we will discuss the distribution of network measures for each dynamical state observed in the combustor.

1. Positively correlated networks

We begin by analyzing the positively correlated networks of the flame intensity oscillations near the end wall of the combustor during the dynamical states of intermittency and thermoacoustic instability. We show the spatial distributions of degree (k) and node strength (s) for different thresholds in Fig. 6.

For $\varepsilon = 0$, we observe that almost all nodes exhibit high k for both intermittency and thermoacoustic instability due to the ubiquitous presence of positive correlations across the window. Hence, both intermittency and thermoacoustic instability display a similar k distribution for $\varepsilon = 0$. On increasing ε to 0.3, weaker correlations are cutoff from the network, revealing regions with stronger interactions. From the k distribution for intermittency, we observe a distinct pattern in the location of nodes with high k. This pattern shows two distinct clusters (found at $y = 10$–19 mm and $y = 20$–34 mm), which exhibit large intensity oscillations during intermittency. These two longitudinal locations correspond to the crests formed by the asymmetrically oscillating jet flames, where heightened flame responses to the acoustic perturbations are recorded. We provide a detailed explanation of the crests formed by the transverse oscillating jet flames in Appendix A.

During thermoacoustic instability, the nodes over the jet flame closest to the end wall along with the aforementioned two clusters exhibit high k. Due to the even larger transverse displacement of the jet flames imparted by the high amplitude shock wave during thermoacoustic instability, the rightmost jet flame impinges with the end wall, resulting in a spike in the local flame intensity. Thus, the nodes lying over the entire jet flame closest to the end wall become highly correlated and possess high k during thermoacoustic instability. For ε beyond 0, high k is observed only during thermoacoustic instability. This difference in k distributions suggests that the majority of the nodes are weakly and strongly coherent during intermittency and thermoacoustic instability, respectively.

The corresponding s distributions show striking differences between intermittency and thermoacoustic instability right from $\varepsilon = 0$. We observe maximum s only during thermoacoustic instability. Furthermore, the pattern of s is nearly the same as the corresponding phase averaged image of CH^* chemiluminescence observed at phase A [see Fig. 3(c)]. Compared to the distribution of k for $\varepsilon = 0$, which seems to capture all the locations covered by the jet flames, the distribution of s captures only the locations housing the highest flame intensity oscillations near the end wall. For successive increments in ε, the spatial locations responsible for the highest flame intensity oscillations are revealed. These spatial locations also happen to exhibit the highest flame intensity oscillations.

In order to examine the size and strength of coherent clusters in the positively correlated networks, we visualize the adjacency matrices in Appendix B. Furthermore, we distinguish the connectivity of nodes inside and outside a coherent cluster using a partial degree analysis discussed in Appendix C.

2. Negatively correlated networks

Now, we study the effect of negative correlations found in the flame intensity oscillations during intermittency and thermoacoustic instability. Negatively correlated networks are constructed following the methodology explained in Sec. III. The distribution of the network measures in the negatively correlated networks enables us to quantify

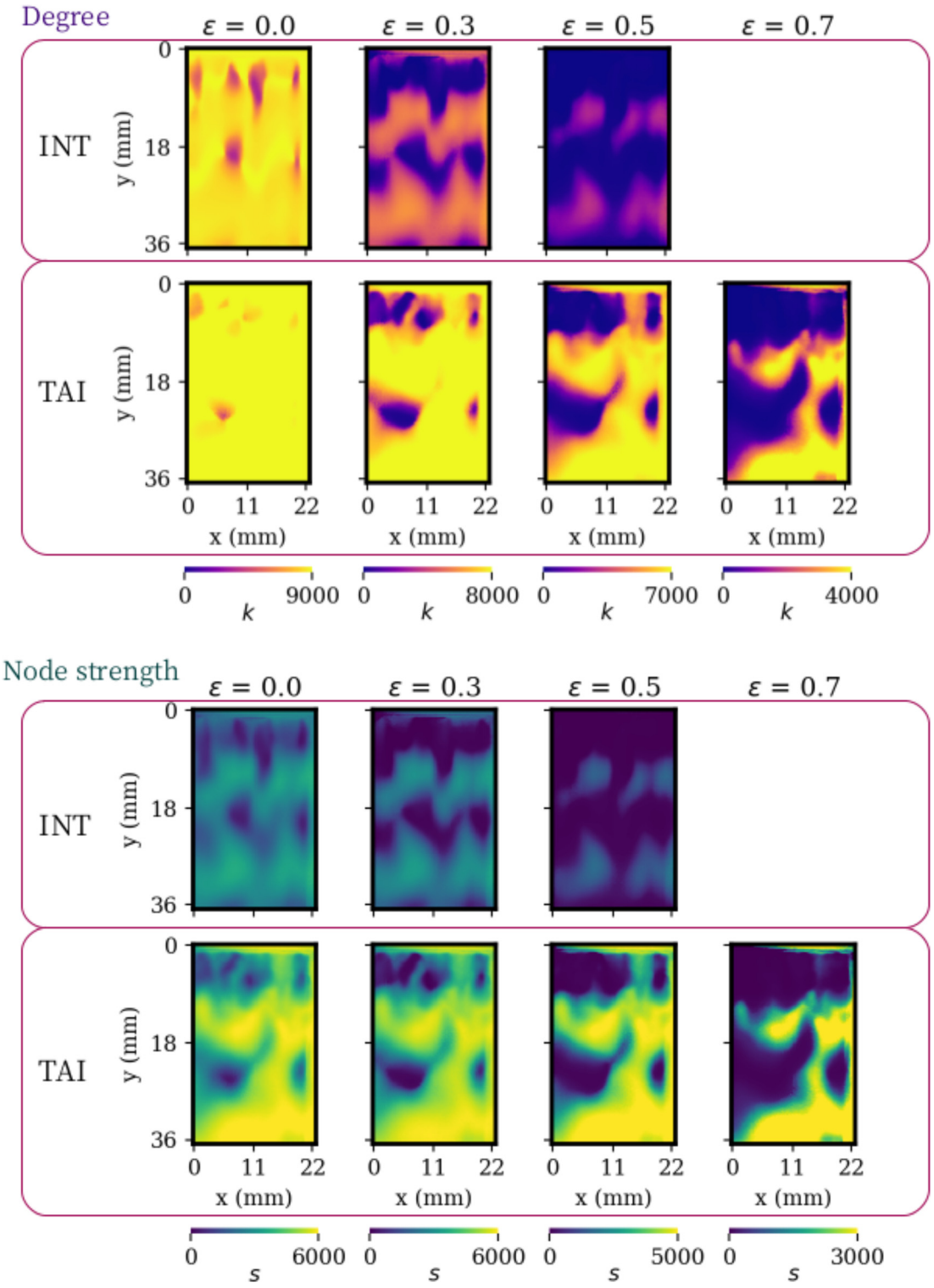

FIG. 6. The spatial distribution of degree (k) and node strength (s) for the positively correlated network during the dynamical states of intermittency (INT) and thermoacoustic instability (TAI) for various correlation thresholds. The patterns in the distributions of k and s across different ε reveal the locations exhibiting varying levels of coherent oscillations. Beyond $\varepsilon = 0.5$, no patterns are visible from the spatial distributions of k and s during intermittency.

the extent of negative correlations in the flame intensity oscillations. In turn, the regions exhibiting negative correlations might indicate local regions, which serve as acoustic power sinks, inhibiting the growth of thermoacoustic oscillations.

As seen in Fig. 4, the range of negative correlations is comparatively lower than the range of positive correlations. As a result, we show the distribution of network measures only for $\varepsilon = 0$ in Fig. 7. For both intermittency and thermoacoustic instability, we observe small islands filled by nodes with high k. These small islands are surrounded by nodes with low k. For both intermittency and thermoacoustic instability, we discern that the distributions of k and s are similar, even using the lowest $\varepsilon = 0$. Furthermore, both network measures only change slightly from intermittency to thermoacoustic instability. The distributions for the negatively correlated networks perfectly complement their corresponding distributions from the positively correlated networks. By this, we mean that nodes having low k (or s) in the positively correlated network have a high k (or s) and vice versa.

The variation of s is largely similar to that of k. This indicates that the locations housing anti-correlated flame intensity oscillations interact uniformly across the entire region. Hence, we conjecture that the uniform nature of these incoherent flame intensity oscillations implies that the oscillations are damped uniformly at these locations, whereas coherent flame intensity oscillations are driven at specific spatial locations (clusters).

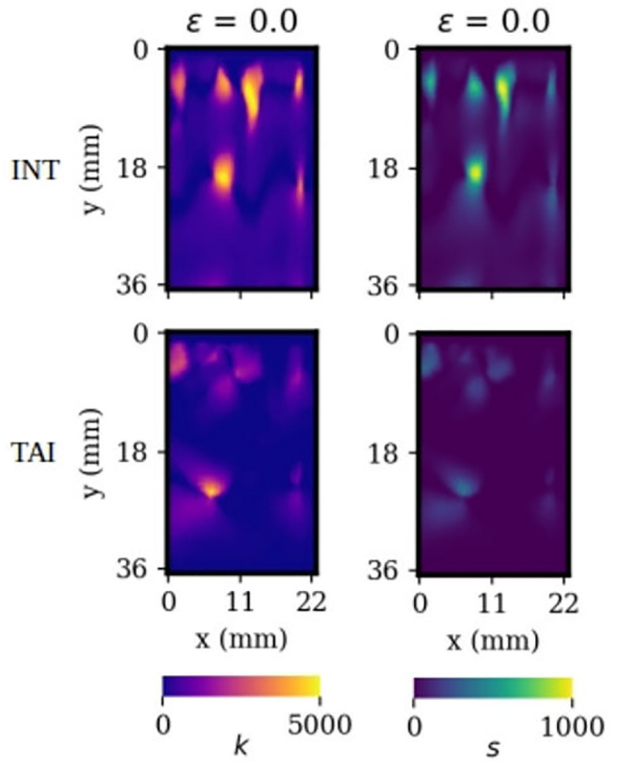

FIG. 7. The spatial distribution of degree (k) and node strength (s) for the negatively correlated network during the different dynamical states for the various correlation thresholds investigated. The sparse presence of negative correlations spread over the spatial domain during different dynamical states is captured by the corresponding distributions of k and s.

All these findings suggest that the spatiotemporal dynamics of the flame intensity oscillations significantly change from intermittency to thermoacoustic instability. Physically, the end wall of the combustor houses the transverse acoustic pressure anti-node. The strong thermoacoustic coupling near the end wall results in higher flame intensities. As a result, the driving of the 1 T mode in the end wall region is higher, leading to widespread coherent flame intensity oscillations during the state of thermoacoustic instability.

Identifying the presence of clusters of coherent flame intensity oscillations does not provide information on the source and pathways underlining the mechanisms sustaining thermoacoustic instability. However, enhanced information on the size and structure of such coherent flame intensity oscillations would enable us to appropriately design control solutions to disrupt the size, structure, and strong coherence in the flame intensity oscillations.

C. Degree correlations and assortative mixing in correlated flame intensity networks

Next, we plot the degree distribution ($P(k)$ vs k) for all the positively and negatively correlated networks in Fig. 8. At the outset, we notice that $P(k)$ of the positively correlated networks constructed by setting an $\varepsilon = 0$ for all dynamical states [Fig. 8(a)] exhibits an increasing trend with k. This implies that there are a large number of spatial locations in the end wall region, which are highly connected among themselves during both intermittency and thermoacoustic instability.

For $\varepsilon > 0$ [Figs. 8(b)–8(d)], we do not see any monotonic behavior in the degree distribution of the positively correlated networks for any dynamical state. We observe that the probability of finding a node having low to intermediate values of k is similar for $\varepsilon = 0.3$ and 0.5. However, the probability of obtaining a high k node increases for thermoacoustic instability due to the widespread coherence in the flame intensity oscillations. However, for the highest ε of 0.7, this probability decreases since the fraction of highly correlated node pairs reduces.

Unlike the positively correlated networks, we obtain a decreasing trend in $P(k)$ for the negatively correlated networks [Fig. 8(e)] for $\varepsilon = 0$. This decreasing trend suggests there exists only a few spatial locations in the flow-field, wherein the flame intensity oscillations are highly negatively correlated among themselves.

The stark differences in the degree distributions of positively and negatively correlated networks motivate us to check the presence of degree-degree correlations. We rely on the measures described in Sec. IV to detect these correlations.

We plot the degree correlation function, $k_{nn}(k)$, against the degree (k) for all the networks investigated in Figs. 9(a)–9(e). We observe that $k_{nn}(k)$ increases with k for both the dynamical states. This trend confirms the presence of degree-degree correlations in the networks, wherein connections are established between nodes of similar degrees. This phenomenon is known as assortative mixing in the network theory.[46]

Specifically, the high degree nodes are preferentially connected with other high degree nodes. Physically, the presence of assortative mixing implies that regions with highly correlated intensity oscillations tend to interact with other regions containing highly correlated intensity oscillations.[46] This leads to the formation of a core group (a cluster)

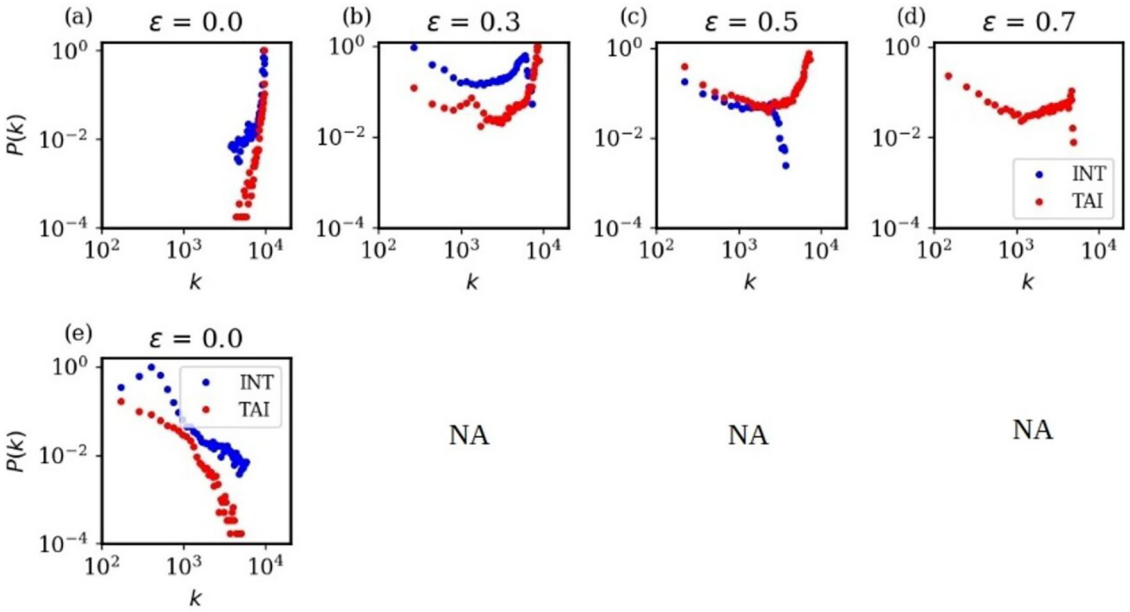

FIG. 8. The degree distribution [$P(k)$ vs k] for (a–d) the positively and (e) negatively correlated networks for each correlation threshold investigated. The degree distributions are shown only for the thresholds investigated. The thresholds for which no patterns are visible in the spatial distributions are labeled non-applicable (NA).

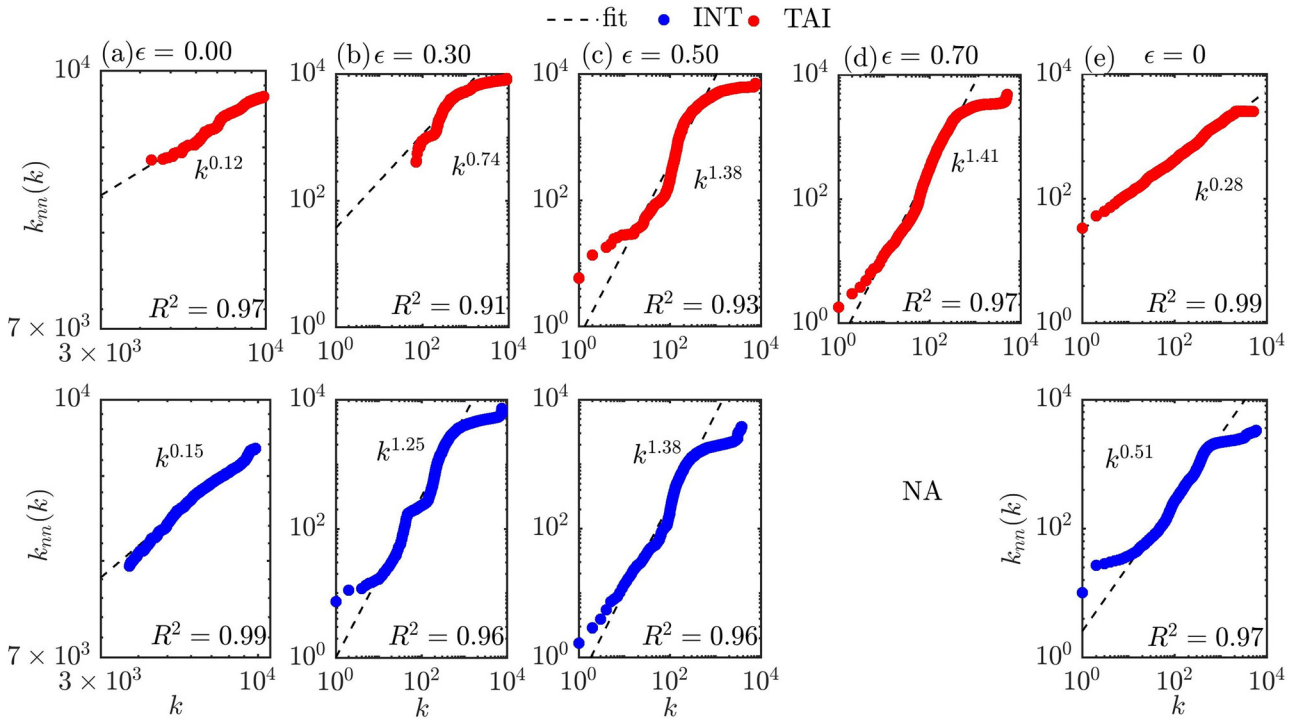

FIG. 9. Log-log plot of the degree correlation function [$k_{nn}(k)$] and degree (k) for (a–d) the positively and (e) negatively correlated networks during intermittency (INT) and thermoacoustic instability (TAI) for different thresholds considered. The increasing trend in the plots suggests the presence of assortative mixing in the positively correlated networks. The degree correlation exponent (μ) and the goodness of the fit (R^2) are indicated. The thresholds for which no patterns are visible in the spatial distributions are labeled non-applicable (NA).

in the network that acts as a "reservoir" for coherent flame intensity oscillations. These reservoirs manifest in the form of clusters in the spatial distributions of degree and node strength in the positively correlated networks. Near the end wall, we find one reservoir of coherent flame intensity oscillations, which spans the majority of the window (see Fig. 6).

To quantify the assortativity in the networks, one can check the presence of a scaling relation[21,49] between $k_{nn}(k)$ and k such that $k_{nn}(k) \sim k^{\mu}$. In the log-log plot of $k_{nn}(k)$ and k shown in Fig. 9, we have fitted $k_{nn}(k)$ as k^{μ}. All the fits are obtained by linear regression characterized by a goodness of the fit (R^2) >90%. We observe all the networks have a $\mu > 0$, confirming the presence of assortativity. The value of μ ranging from 0.12 to 1.41 indicates the different assortative nature in the networks examined in this study. In comparison, the internet network, mobile phone call network, and science collaboration network have μ values of 0.56, 0.33, and 0.16, respectively.[21] The value of $\mu > 1$ is indicative of the stronger assortative nature in some of the positively correlated networks.

The presence of assortativity in the networks indicates that any node is most likely connected to other nodes with similar degree. Newman[46] reported that the removal of high degree nodes in an assortatively mixed network is an inefficient way to destroy the network connectivity considerably. Hence, we can hypothesize that any passive control strategies targeting the regions with high k in this combustor may be inefficient in suppressing thermoacoustic oscillations. Any successful control action for suppressing the oscillations might warrant overwhelming changes to the engine design and necessitate several full-scale tests. However, dedicated experiments need to be performed to verify this hypothesis.

Thus, utilizing positively and negatively correlated networks constructed for various correlation thresholds, we quantify the interactions among the local flame intensity oscillations. We identify that majority of the spatial locations are positively correlated as exemplified by the correlation weights and network measures. Furthermore, we find significant differences in the interactions and the network structure of positively and negatively correlated flame intensity networks.

VI. CONCLUSIONS

We have performed a weighted spatial network analysis of the local flame intensity oscillations acquired from the CH^* chemiluminescence fields during the transition from intermittency to thermoacoustic instability in a multi-element 2D model rocket combustor. The spatiotemporal dynamics has been studied near the end wall region, where the flame intensity oscillations are the highest. Our analysis unraveled fundamental differences in the connectivity of positively and negatively correlated spatial networks. The network measures revealed the differences in the coherence in the flame intensity oscillations during intermittency and thermoacoustic instability. We identified that many spatial locations are populated by high degree and high node strength during thermoacoustic instability, translating to highly coherent flame intensity oscillations. Such network measures can be valuable metrics for testing the validity of computational simulations. Finally, we also discovered the presence of assortative mixing leading to the formation of reservoirs of coherent flame intensities. To the best of our knowledge, this is the first evidence of assortative mixing in turbulent reactive flows.

Validation of computational simulations with experimental data, especially for high-pressure and high power-density devices has traditionally been performed by comparing point measurements of pressure (or other variables) measured in the experiment temporally. In rocket combustors, where large optical access for high-speed imaging or laser-based diagnostics is challenging, very few studies available in the open literature have performed comparison of spatiotemporal data.[16,50–52] In these studies, path integrated chemiluminescence measurements were compared with heat release rate from simulations using direct comparison of broad coherent flow features derived from time-averaged or phase-averaged images using broadband or filtered chemiluminescence measurements. Additional comparison was also performed by reconstructing and comparing prominent features in the flow, sorted by the highest energy content using proper orthogonal decomposition, using experimental and computational data. This comparison provided valuable insight into the mechanisms promoting combustion instability in the experiments, but the qualitative nature of the comparison was insufficient for verification and validation of the numerical results. Where more quantitative comparisons are available, these are primarily made using temporal history of pressure measurements with wall mounted sensors.[53] The amplitudes of the experimentally obtained pressure oscillations (and other directly measured quantities from experiments) and their dominant frequencies are compared with that of numerical simulations. Obtaining a match in only these features might be inadequate and may not replicate or predict the dynamics occurring in experiments correctly. The detailed features of the spatiotemporal data obtained from experiments, albeit very useful, are largely neglected in this validation process. We propose using the spatial variation of network measures (degree and node strength) along with their distributions on the data obtained from experiments and matching numerical simulations to tighten the validation process. Furthermore, the validation of simulations that aim to mimic the experimental observations in a rocket or other high-power combustion devices can be augmented by comparing the size, structure, and extent of coherence in the flame intensity oscillations.

ACKNOWLEDGMENTS

The authors gratefully acknowledge the funding provided by AFOSR under Award No. FA2386–18-1–4116 (Grant Program Manager: Lt Col Sheena Winder). This work was also funded by the IoE initiative (No. SB/2021/0845/AE/MHRD/002696) of IIT Madras and the Government of India.

R.I.S. thanks Dr. V. Sankaran (AFRL) for initiating this project. P.K. acknowledges Ms. Induja Pavithran and Dr. Samadhan Pawar (both from IIT Madras) for the stimulating discussions on the analysis. We thank Mr. Michael Orth and Professor Timothee Pourpoint for performing the experimental campaign at Purdue University. Finally, we thank the reviewers whose critical comments raised the quality of our manuscript.

AUTHOR DECLARATIONS

Conflict of Interest

The authors have no conflicts of interest to disclose.

DATA AVAILABILITY

The data that support the findings of this study are available from the corresponding author upon reasonable request.

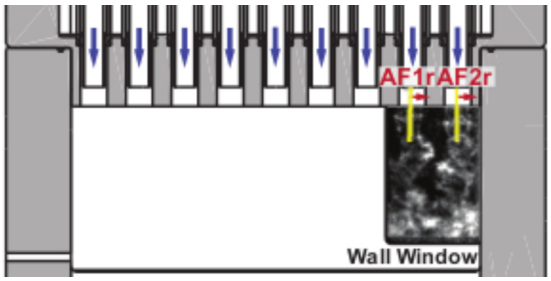

FIG. 10. The selected portion of the jet flame (i.e., half of the width of the jet flame) overlaid on the representative CH* chemiluminescence image obtained from the end wall window.

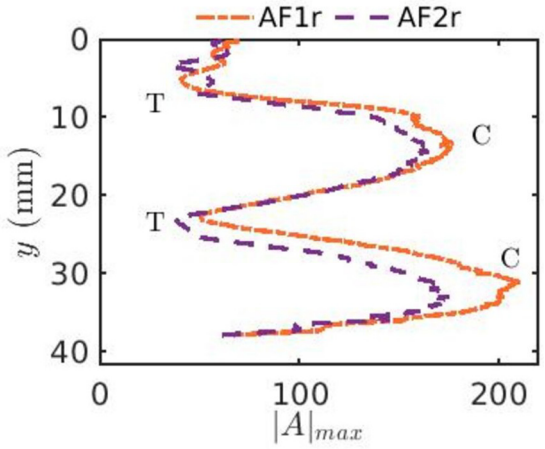

FIG. 11. The flame response along the longitudinal direction characterized by the amplitude of the dominant mode of the oscillations of pixel intensities summed across the transverse direction for the half width of the left flame (AF1r) and the right flame (AF2r). The crests and troughs in the flame response are indicated with C and T, respectively.

APPENDIX A: JET FLAME RESPONSE TO TRANSVERSE ACOUSTIC OSCILLATIONS ALONG THE LONGITUDINAL DIRECTION

It is well-known from past studies that a flame in the presence of transverse thermoacoustic oscillations responds differently than that observed for the longitudinal oscillations.[54] In this combustor, the turbulent jet flames are largely in the longitudinal direction and are susceptible to transverse velocity perturbations whenever an acoustic wave passes through them. Hence, it is interesting to examine the response of the flames to self-excited transverse oscillations in the longitudinal direction.

Across the width of the jet flame, a varicose or sinuous mode of the jet flame would exhibit in-phase or out-of-phase oscillations, respectively, in the flame intensity fluctuations obtained from both halves of the jet flame. In this study, we found that each jet flame exhibits sinuous oscillations. When we select the entire width of the jet flame for the local flame intensity calculations, we were not able to make this distinction in the oscillatory motion of the flame due to superposition effects along both halves of the jet flame. Hence,

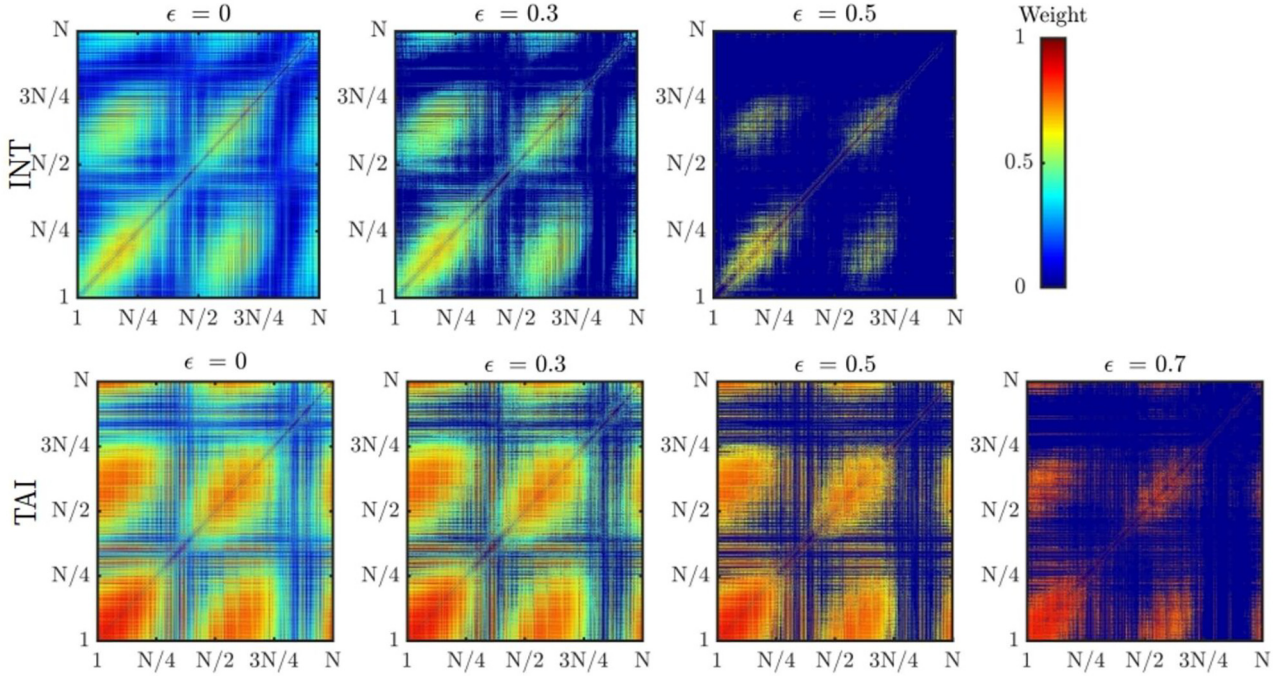

FIG. 12. Visualization of the adjacency matrix for the positively correlated networks during intermittency (INT) and thermoacoustic instability (TAI) for different thresholds considered. Large weights among neighboring nodes are indicative of the presence of clusters.

we selected just a half of the jet flame (see Fig. 10) to detect the type of vortex shedding (sinuous or varicose) exhibited by the flame front. The time series of the local flame intensity fluctuations is obtained by summing up the flame intensities at each pixel across half-width of the jet flame for the right half of left jet flame (AF1r) and right half of right jet flame (AF2r) as shown in Fig. 10.

In Fig. 11, we plot the variation of the amplitude of the dominant mode of the local flame intensity oscillations obtained from the half-width of the flame in the longitudinal direction (see Fig. 10). From Fig. 11, we observe that the spectral amplitude of the dominant mode through FFT of such local flame intensity fluctuations shows oscillatory response with the presence of multiple crests (C) and troughs (T) along the flame length. Such an oscillatory response of the flame is a combined result of the globally unstable nature of the pre-heated reacting flow-field[13,55] in the presence of a transverse acoustic field in the combustor. Near the injector, the flame response is controlled by flame anchoring while at the downstream locations, the flame response is largely controlled by the dissipation of vortical

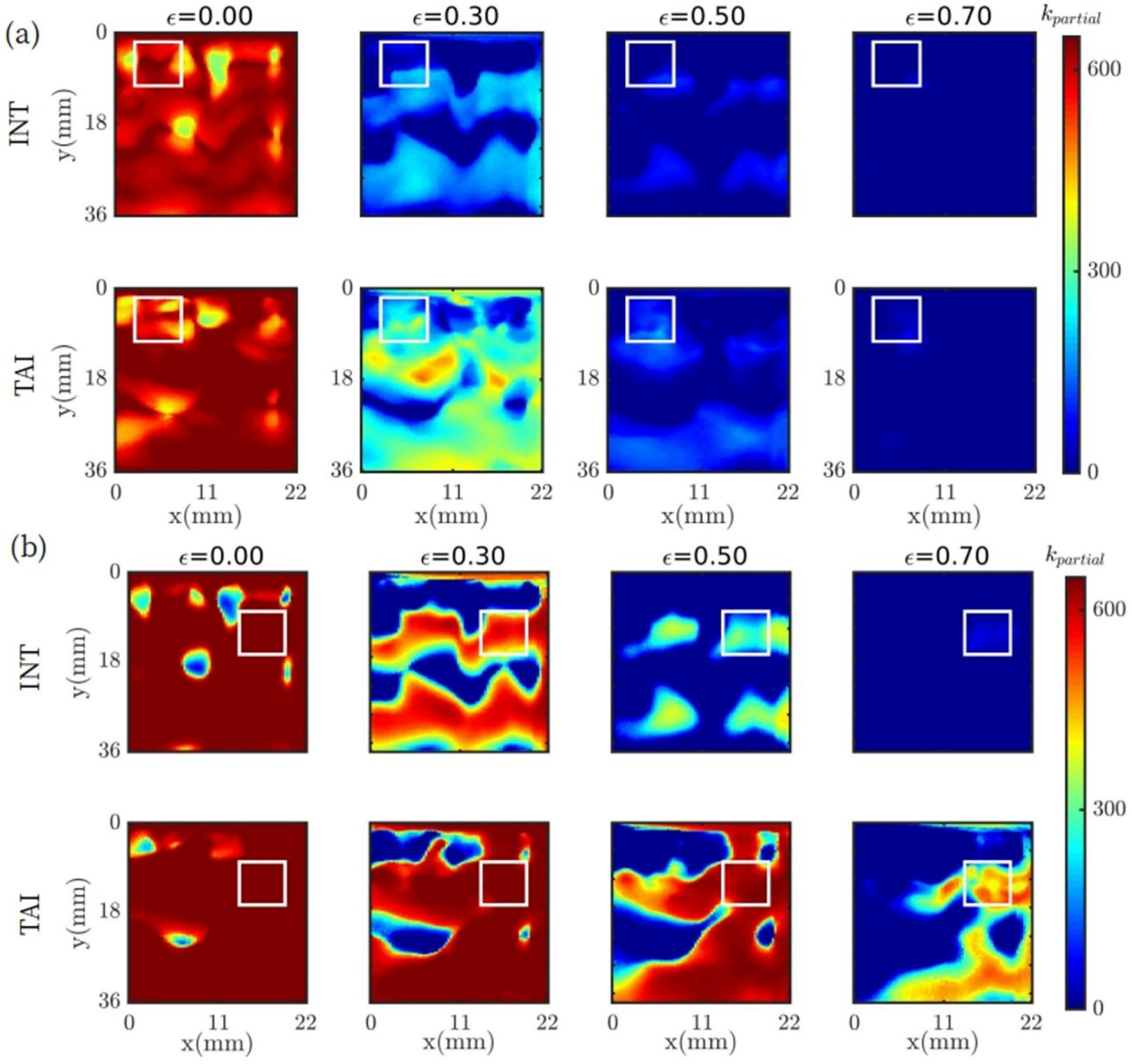

FIG. 13. Spatial distribution of the partial degree ($k_{partial}$) evaluated for the connections originating from the nodes located inside (a) box 1 and (b) box 2 for the positively correlated networks during intermittency (INT) and thermoacoustic instability (TAI) for different thresholds considered. Boxes 1 and 2 are chosen to be representative of an incoherent and coherent region in the flow field, respectively.

disturbances and other secondary flows along the boundary of the flame surfaces.[56] Thus, each flame exhibits varying dominant amplitudes along its length.

We notice a similar response for the AF1r and AF2r jet flames with two crests. The first crest in the flame responses occurs around 14 mm downstream of the injector head. In addition to the flame anchoring effects, the flame response at this location is supplemented from the strong interactions from the transverse acoustic wave and the neighboring sides of the flames through merging effects and the resulting impingement with the wall. The flame that is compact near the injector spreads out at the downstream locations. This leads to enhanced mixing and subsequently higher flame intensities. Conversely, the second crest around 32 mm downstream of the injector is a consequence of the secondary flows caused by vortical dissipation along the flame surfaces leading to better mixing and autoignition of propellants.[57] Downstream of the second crest, boundary effects of the converging nozzle section dominate.[58] Thus, the response of the flame to transverse acoustic perturbations is non-uniform along the longitudinal direction of the combustor.

APPENDIX B: VISUALIZATION OF ADJACENCY MATRIX

We visualize the corresponding adjacency matrices (of size $N \times N = 9828 \times 9828$) for the positively correlated networks during intermittency and thermoacoustic instability in Fig. 12. Throughout all the adjacency matrices, we can observe the strong linkages among the neighboring nodes identified by the spots carrying high weights. The weights of these spots increase during the transition from intermittency to thermoacoustic instability. The size and color of these characteristic spots depict the extent of coherence in the clusters identified in the spatial distributions (Fig. 6).

APPENDIX C: PARTIAL DEGREE ANALYSIS

In order to demonstrate the enhanced connectivity of nodes belonging to a coherent cluster, we repeat the network analysis for small localized regions in the flow-field. Only the connections from the localized region (boxes 1 and 2) are considered. Boxes 1 and 2 are chosen to be representative of incoherent and coherent regions, respectively. The size of the box is chosen to approximately span the width of one of the jet flames in the window. Then, we evaluated the partial degree, i.e., the number links connected to the selected region housing a small fraction of nodes in the entire network.

In Fig. 13, we show the obtained partial degree distribution ($k_{partial}$) for the connections emerging from two boxes (boxes 1 and 2) from the positively correlated networks constructed during intermittency and thermoacoustic instability. For $\varepsilon = 0$, all the distributions of $k_{partial}$ are nearly similar. However, upon increasing the ε to 0.3 and above, we observe that only the distributions of $k_{partial}$ associated with box 2 show a large number of connections. This analysis is further proof of the box 2 region belonging to a coherent cluster, whereas box 1 belongs to an incoherent region. In summary, the chosen two boxes demonstrate the presence (or lack of) of strong clustering behavior and widespread connectivity due to high (or low) coherence in the flame intensity oscillations.

REFERENCES

[1]G. P. Sutton, *History of Liquid Propellant Rocket Engines* (AIAA, 2006).
[2]M. L. Dranovsky, *Combustion Instabilities in Liquid Rocket Engines: Testing and Development Practices in Russia* (AIAA, 2007).
[3]Y. Nunome, T. Onodera, M. Sasaki, T. Tomita, K. Kobayashi, and Y. Daimon, "Combustion instability phenomena observed during cryogenic hydrogen injection temperature ramping tests for single coaxial injector elements," AIAA Paper No. 2011-6027, 2011.
[4]D. Watanabe, H. Manako, T. Onga, T. Tamura, K. Ikeda, and M. Isono, "Combustion stability improvement of LE-9 engine for booster stage of H3 launch vehicle," Mitsubishi Heavy Ind. Tech. Rev. **53**, 28 (2016); available at https://www.mhi.co.jp/technology/review/pdf/e534/e534028.pdf
[5]S. D. Heister, W. E. Anderson, T. L. Pourpoint, and R. J. Cassady, *Rocket Propulsion* (Cambridge University Press, 2019), Vol. 47.
[6]W. E. Anderson and V. Yang, *Liquid Rocket Engine Combustion Instability* (Progress in Astronautics and Aeronautics, AIAA, 1995), Vol. 169.
[7]W. A. Sirignano, "Driving mechanisms for combustion instability," Combust. Sci. Tech. **187**, 162–205 (2015).
[8]F. Culick and P. Kuentzmann, "Unsteady motions in combustion chambers for propulsion systems," NATO Research and Technology Organization Neuilly-Sur-Seine (France), 2006.
[9]D. T. Harrje, "Liquid propellant rocket combustion instability," Report No. NASA SP-194, 1972.
[10]A. Urbano, Q. Douasbin, L. Selle, G. Staffelbach, B. Cuenot, T. Schmitt, S. Ducruix, and S. Candel, "Study of flame response to transverse acoustic modes from the LES of a 42-injector rocket engine," Proc. Combust. Inst. **36**, 2633–2639 (2017).
[11]J. S. Hardi, S. K. Beinke, M. Oschwald, and B. B. Dally, "Coupling of cryogenic oxygen–hydrogen flames to longitudinal and transverse acoustic instabilities," J. Propul. Power **30**, 991–1004 (2014).
[12]T. C. Lieuwen, *Unsteady Combustor Physics* (Cambridge University Press, 2012).
[13]B. Emerson, J. O'Connor, M. Juniper, and T. Lieuwen, "Density ratio effects on reacting bluff-body flow field characteristics," J. Fluid Mech. **706**, 219–250 (2012).
[14]M. Oschwald and B. Knapp, "Investigation of combustion chamber acoustics and its interaction with LO_X/H_2 spray flames," Prog. Propul. Phys. **1**, 205–224 (2009).
[15]M. Sliphorst, G. Stefan, B. Knapp, and M. Oschwald, "Combustion instability coupling mechanisms between acoustics and LO_x/CH_4 spray flames," AIAA Paper No. 2011-327, 2011.
[16]C. J. Morgan, K. J. Shipley, and W. E. Anderson, "Comparative evaluation between experiment and simulation for a transverse instability," J. Propul. Power **31**, 1696–1706 (2015).
[17]C. Rey, S. Ducruix, P. Scouflaire, F. Richecoeur, L. Vingert, and S. Candel, "High frequency combustion instabilities associated with collective interactions in liquid propulsion," AIAA Paper No. 2004-3518, 2004.
[18]F. Richecoeur, P. Scouflaire, S. Ducruix, and S. Candel, "High-frequency transverse acoustic coupling in a multiple-injector cryogenic combustor," J. Propul. Power **22**, 790–799 (2006).
[19]W. Armbruster, J. S. Hardi, and M. Oschwald, "Flame-acoustic response measurements in a high-pressure, 42-injector, cryogenic rocket thrust chamber," Proc. Combust. Inst. **38**, 5963–5970 (2021).
[20]R. I. Sujith and V. R. Unni, "Complex system approach to investigate and mitigate thermoacoustic instability in turbulent combustors," Phys. Fluids **32**, 061401 (2020).
[21]A. L. Barabási *et al.*, *Network Science* (Cambridge University Press, 2016).
[22]Y. Zou, R. V. Donner, N. Marwan, J. F. Donges, and J. Kurths, "Complex network approaches to nonlinear time series analysis," Phys. Rep. **787**, 1–97 (2019).
[23]K. Taira, A. G. Nair, and S. L. Brunton, "Network structure of two-dimensional decaying isotropic turbulence," J. Fluid Mech. **795**, 1–11 (2016).
[24]R. I. Sujith and S. A. Pawar, *Thermoacoustic Instability: A Complex Systems Perspective* (Springer Nature, 2021).
[25]M. Murugesan and R. I. Sujith, "Combustion noise is scale-free: Transition from scale-free to order at the onset of thermoacoustic instability," J. Fluid Mech. **772**, 225–245 (2015).

[26]V. Godavarthi, V. R. Unni, E. A. Gopalakrishnan, and R. I. Sujith, "Recurrence networks to study dynamical transitions in a turbulent combustor," Chaos **27**, 063113 (2017).
[27]H. Gotoda, H. Kinugawa, R. Tsujimoto, S. Domen, and Y. Okuno, "Characterization of combustion dynamics, detection, and prevention of an unstable combustion state based on a complex-network theory," Phys. Rev. Appl. **7**, 044027 (2017).
[28]T. Kobayashi, S. Murayama, T. Hachijo, and H. Gotoda, "Early detection of thermoacoustic combustion instability using a methodology combining complex networks and machine learning," Phys. Rev. Appl. **11**, 064034 (2019).
[29]P. Kasthuri, I. Pavithran, A. Krishnan, S. A. Pawar, R. I. Sujith, R. Gejji, W. E. Anderson, N. Marwan, and J. Kurths, "Recurrence analysis of slow–fast systems," Chaos **30**, 063152 (2020).
[30]V. R. Unni, A. Krishnan, R. Manikandan, N. B. George, R. I. Sujith, N. Marwan, and J. Kurths, "On the emergence of critical regions at the onset of thermoacoustic instability in a turbulent combustor," Chaos **28**, 063125 (2018).
[31]A. Krishnan, R. Manikandan, P. Midhun, K. Reeja, V. Unni, R. I. Sujith, N. Marwan, and J. Kurths, "Mitigation of oscillatory instability in turbulent reactive flows: A novel approach using complex networks," Euro Phys. Lett. **128**, 14003 (2019).
[32]A. Krishnan, R. I. Sujith, N. Marwan, and J. Kurths, "Suppression of thermoacoustic instability by targeting the hubs of the turbulent networks in a bluff body stabilized combustor," J. Fluid Mech. **916**, A20 (2021).
[33]A. Krishnan, R. I. Sujith, N. Marwan, and J. Kurths, "On the emergence of large clusters of acoustic power sources at the onset of thermoacoustic instability in a turbulent combustor," J. Fluid Mech. **874**, 455–482 (2019).
[34]T. Hashimoto, H. Shibuya, H. Gotoda, Y. Ohmichi, and S. Matsuyama, "Spatiotemporal dynamics and early detection of thermoacoustic combustion instability in a model rocket combustor," Phys. Rev. E **99**, 032208 (2019).
[35]C. Aoki, H. Gotoda, S. Yoshida, and S. Tachibana, "Dynamic behavior of intermittent combustion oscillations in a model rocket engine combustor," J. Appl. Phys. **127**, 224903 (2020).
[36]S. Shima, K. Nakamura, H. Gotoda, Y. Ohmichi, and S. Matsuyama, "Formation mechanism of high-frequency combustion oscillations in a model rocket engine combustor," Phys. Fluids **33**, 064108 (2021).
[37]A. Karmarkar, A. Tyagi, S. Hemchandra, and J. O'Connor, "Impact of turbulence on the coherent flame dynamics in a bluff-body stabilized flame," Proc. Combust. Inst. **38**, 3067–3075 (2021).
[38]P. Kasthuri, S. A. Pawar, R. Gejji, W. Anderson, and R. I. Sujith, "Coupled interaction between acoustics and unsteady flame dynamics during the transition to thermoacoustic instability in a multi-element rocket combustor," Combust. Flame **240**, 112047 (2021).
[39]C. A. Fugger, R. M. Gejji, J. E. Portillo, Y. Yu, R. P. Lucht, and W. E. Anderson, "A model combustor for studying a reacting jet in an oscillating crossflow," Rev. Sci. Instrum. **88**, 065112 (2017).
[40]T. L. Fuller, "Review of chemiluminescence as an optical diagnostic tool in high pressure unstable rockets," Ph.D. thesis, Purdue University, 2015.
[41]M. J. Bedard, T. L. Fuller, S. Sardeshmukh, and W. E. Anderson, "Chemiluminescence as a diagnostic in studying combustion instability in a practical combustor," Combust. Flame **213**, 211–225 (2020).
[42]M. R. Orth, C. Vodney, T. Liu, W. Z. Hallum, T. L. Pourpoint, and W. E. Anderson, "Measurement of linear growth of self-excited instabilities in an idealized rocket combustor," AIAA Paper No. 2018-1185, 2018.
[43]P. Kasthuri, I. Pavithran, S. A. Pawar, R. I. Sujith, R. Gejji, and W. E. Anderson, "Dynamical systems approach to study thermoacoustic transitions in a liquid rocket combustor," Chaos **29**, 103115 (2019).
[44]R. Gejji, A. I. Lemcherfi, R. Strelau, C. D. Slabaugh, and W. E. Anderson, "Combustion response of shear coaxial injectors to transverse combustion instabilities," AIAA Paper No. 2020-0424, 2020.
[45]A. Barrat, M. Barthélemy, and A. Vespignani, "The effects of spatial constraints on the evolution of weighted complex networks," J. Stat. Mech. **2005**, P05003.
[46]M. E. Newman, "Assortative mixing in networks," Phys. Rev. Lett. **89**, 208701 (2002).
[47]V. Nair, G. Thampi, and R. I. Sujith, "Intermittency route to thermoacoustic instability in turbulent combustors," J. Fluid Mech. **756**, 470–487 (2014).
[48]M. Stöhr, R. Sadanandan, and W. Meier, "Phase-resolved characterization of vortex–flame interaction in a turbulent swirl flame," Exp. Fluids **51**, 1153–1167 (2011).
[49]R. Pastor-Satorras, A. Vázquez, and A. Vespignani, "Dynamical and correlation properties of the internet," Phys. Rev. Let. **87**, 258701 (2001).
[50]J. S. Hardi, W. Zach Hallum, C. Huang, and W. E. Anderson, "Approaches for comparing numerical simulation of combustion instability and flame imaging," J. Propul. Power **32**, 279–294 (2016).
[51]J. Hardi, S. Gröning, S. Webster, S. Beinke, D. Suslov, and M. Oschwald, "Review of experimental test cases for modelling high frequency combustion instability," AIAA Paper No. 2016-4893, 2016.
[52]S. K. Beinke, J. S. Hardi, D. T. Banuti, S. Karl, B. B. Dally, and M. Oschwald, "Experimental and numerical study of transcritical oxygen-hydrogen rocket flame response to transverse acoustic excitation," Proc. Combust. Inst. **38**, 5979–5986 (2021).
[53]M. E. Harvazinski, C. Huang, V. Sankaran, T. W. Feldman, W. E. Anderson, C. L. Merkle, and D. G. Talley, "Coupling between hydrodynamics, acoustics, and heat release in a self-excited unstable combustor," Phys. Fluids **27**, 045102 (2015).
[54]J. O'Connor, V. Acharya, and T. Lieuwen, "Transverse combustion instabilities: Acoustic, fluid mechanic, and flame processes," Prog. Energy Combust. Sci. **49**, 1–39 (2015).
[55]S. Suresha, R. I. Sujith, B. Emerson, and T. Lieuwen, "Nonlinear dynamics and intermittency in a turbulent reacting wake with density ratio as bifurcation parameter," Phys. Rev. E **94**, 042206 (2016).
[56]S. Shanbhogue, D.-H. Shin, S. Hemchandra, D. Plaks, and T. Lieuwen, "Flame-sheet dynamics of bluff-body stabilized flames during longitudinal acoustic forcing," Proc. Combust. Inst. **32**, 1787–1794 (2009).
[57]A. M. Blacker, "Characterization of lifted flame behavior in a multi-element rocket combustor," Ph.D. thesis, Purdue University, 2019.
[58]R. Gejji, W. E. Anderson, and B. L. Austin, "Transverse combustion instabilities in a high pressure multi-element combustor," AIAA Paper No. 2109-3947, 2019.